



Schweizerischer Erdbebendienst
Service Sismologique Suisse
Servizio Sismico Svizzero
Swiss Seismological Service

ETH zürich

SITE CHARACTERIZATION REPORT

SCAS2: Camedo (TI), Stausee

Paolo Bergamo, Agostiny Lontsi, Donat Fäh



Last modification: 24.10.2019

Schweizerischer Erdbebendienst (SED)
Service Sismologique Suisse
Servizio Sismologico Svizzero
Servizi da Terratrembels Svizzer

ETH Zurich
Sonnegstrasse 5
8092 Zuerich
Schweiz
paolo.bergamo@sed.ethz.ch

Contents

	Section	Page
	Summary	3
1.	Introduction	4
2.	Geological setting	4
3.	Active seismic measurements	6
3.1	Equipment	6
3.2	Geometry of the acquisition array	7
3.3	Acquisition	8
3.4	Processing	9
3.4.1	<i>Pre-processing</i>	9
3.4.2	<i>Refraction processing and interpretation</i>	10
3.4.3	<i>Rayleigh wave data fk processing</i>	12
3.4.4	<i>WaveDecActive</i>	13
4.	Passive seismic measurements	15
4.1	Acquisition	15
4.2	Processing	15
5.	Inversion of Rayleigh wave data	18
5.1	Inversion target	19
5.2	Parameterization of the subsurface	20
5.3	Inversion results	20
6.	Interpretation of the velocity profiles	22
6.1	Velocity profiles	22
6.2	Quarter-wavelength representation	23
6.3	SH amplification function	25
7.	Conclusions	25

Summary

The new SSMNet station SCAS2 has been installed in Centovalli (TI) at the hamlet of Camedo, on the southern shore of the artificial lake (lago di Palagnedra) originating from the dam of Palagnedra on the Melezza river. It is operating since 5.10.2016. Active seismic measurements, as well as a single-station noise recording survey, were performed to characterize the subsurface structure beneath the station. The site is characterized by a high fundamental frequency (14.65 Hz) which can be related to the surficial interface between weathered and the intact gneisses. According to our measurements, the boundary should be located at a depth of about 11 m.

The estimated V_{S30} value is 768 m/s, which places the site at the upper bound of B class both for SIA261 (SIA, 2014) and Eurocode 8 (CEN, 2004) norms. The engineering bedrock (H800) is estimated at 5 m depth (interface between unconsolidated sediments above and weathered rock below).

1. Introduction.

In the framework of the second phase of the Swiss Strong Motion Network (SSMNet) renewal project, a new station, labelled as SCAS2, was installed in Centovalli (TI), at the hamlet of Camedo, on the southern shore of the artificial lake (lago di Palagnedra) originating from the dam of Palagnedra on the Melezza river (Figure 1). The station is operating since 5.10.2016. According to the available geological information (Swisstopo, 2019), the station rests on few meters of unconsolidated sediments, in turn lying on a stiff gneiss bedrock. The location of SCAS2 on an irregular flank of a mountain with expected shallow bedrock, make the site particularly suitable for the execution of an active seismic survey. Therefore, multichannel analysis of surface waves (MASW, Park et al. 1999) as well as P- and SH-waves refraction surveys (Redpath, 1973) were carried out for the purpose of seismic characterization of the site; these measurements were complemented by a single-station H/V measurement.

2. Geological setting

The site hosting SCAS2 lies along the valley of the Melezza, a deeply incised valley extending approximately in west-east direction at the border between Canton Ticino and Piemonte (Italy). The river Melezza is stopped a couple of kilometers downstream from SCAS2 by a dam (diga di Palagnedra), thus originating an artificial lake (lago di Palagnedra). The bedrock of the valley is constituted by gneisses, in general covered by few meters (or few tens of meters) of either moraine or unconsolidated sediments (Figure 2; Swisstopo 2018). The cover is not present along the valley center or along the many streams converging towards the central axis of the valley, where the gneisses are outcropping. The area hosts also a dense network of faults, extending in either east-west or north-south direction; the fault closest to SCAS2 is no more than 100 meters away. According to the Swiss Geological Atlas, the exact location of SCAS2 is on a patch of unconsolidated sediments surrounded by outcropping gneisses (Figure 2).



Figure 1 – Geographical location of station SCAS2 (© 2019 Swisstopo).

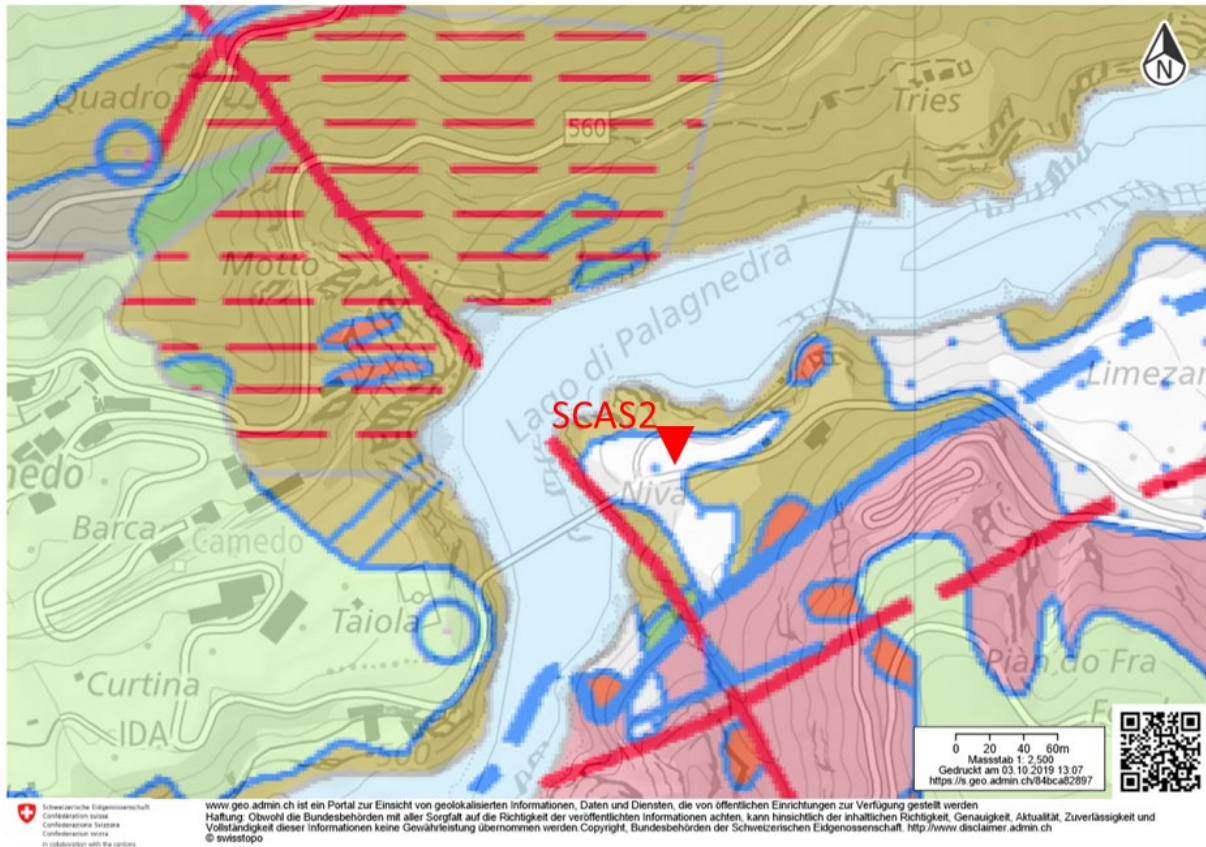


Figure 2 – Location of station SCAS2 on the 1:25000 Swisstopo geological atlas (© 2018 Swisstopo). The color legend is the following: light brown = heterogeneous gneisses; white = unconsolidated deposits; light green = moraine; pink = gneiss with two micas, alkaline feldspar and plagioclase, or with a flaser texture; continuous red lines: faults; dashed red lines = tectonized zone; thick blues lines = overthrust.

3. Active seismic measurements

Station SCAS2 is located on a small embankment of unconsolidated sediments on the southern shore of the Palagnedra artificial lake. The active seismic array was deployed along the diagonal of this area (therefore stretching approximately in west-east direction, Figure 3), to maximize its length and therefore the wavelength coverage.

For the sake of a comprehensive subsurface characterization, multichannel analysis of surface waves (MASW; Park et al., 1999) and P-/SH-wave refraction (Redpath, 1973) surveys were conducted.

3.1 Equipment

We used three sets of eight three-component geophones (4.5 Hz corner frequency). Each geophone set was connected to a Geode datalogger; the three Geodes were coupled for time synchronization. The seismic source was a 5-kg sledgehammer, hitting at four (out of five) source locations (src1-4; Figure 3) a wedge-shaped metallic frame, for SH- and P-wave excitation. The plate is an isosceles right triangle: the hypotenuse is placed on the ground, and coupled to it with spikes penetrating the soil. The catheti are oriented orthogonally to the geophone spread, and alternately hit with the hammer

(see top of Figure 4). As for the last source point (src5), a flat metal plate was employed, for P-SV wave excitation: the hammer was released vertically on the plate.

The synchronization between the traces recorded by the geophones and the seismic source was ensured by a trigger device fastened to the hammer handle.



Figure 3 – Map representing the position of the targeted station (SCAS2), of the active seismic line and of the noise recording sensor (labelled H/V; © 2019 Swisstopo).

3.2 Geometry of the acquisition array

The seismic line was constituted by 24 3-component receivers, aligned at regular intervals of 1 m, for a total length of 23 m. The geophones were laid on the soil, with metal spikes ensuring a firm coupling with the ground (Figure 4).

As earlier anticipated, MASW and P-/SH- wave refraction measurements were performed. As for refraction surveys, the sources were placed at four locations along the receivers' line: at the east end, at one and two thirds of the spread, and at the west end (src1-4, Figure 3). An additional MASW-only shooting position was placed east of the array, 8 m from the closest geophone (Figure 3, src5). Due to logistical constraints (a small scarp at the western edge of the line), it was not possible to deploy the source in a symmetrical position west of the array (off-end shooting, typical configuration for MASW acquisition: see for instance Ivanov et al., 2004).



Figure 4 – Geophone array in place.

3.3 Acquisition

The time-sampling parameters adopted for both MASW and refraction acquisitions were the following: sampling interval = $62.5 \mu\text{s}$, record length = 1.5 s, pre-trigger delay = -0.05 s. At the source points src1-4, 10 hammer blows were successively shot, five for each side of the wedge plate. As earlier anticipated, in src5 only 10 vertical hits were struck, on a flat metal plate. For each hammer blow, the recordings from all geophones were saved in a separate .sg2 file. In Figure 5, we show the

seismic sections for the vertical, transversal and longitudinal components of the geophones, originating from a vertical blow on the flat metal plate at src5 (top row), and from a hammer blow on a slant face of the wedge plate at src1 (bottom row).

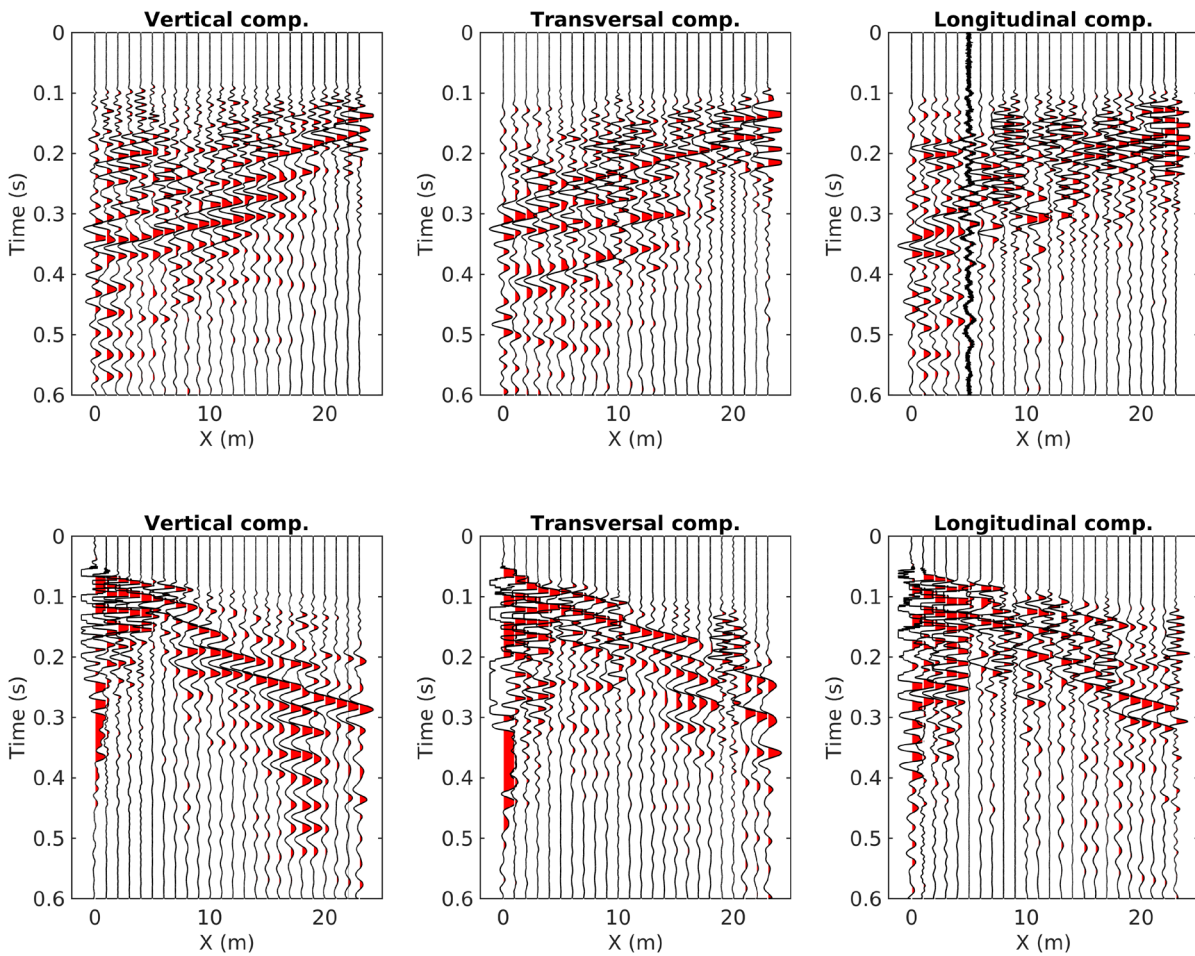


Figure 5 – Seismic traces for the vertical, transversal and longitudinal components of the geophones, originating from a vertical blow on the flat metal plate at src5 (top row), and from a hammer blow on a slant face of the wedge plate at src1 (bottom row). The X coordinate refers to the distance from the westernmost receiver.

3.4 Processing

3.4.1 Pre-processing

As for seismic refraction acquisitions (src1-4), seismic traces generated by different shots, with the same seismic source at the same location (5 sets for each configuration), were summed - or stacked - in time domain. This was done to enhance the coherent seismic events generated by the controlled seismic source, and at the same time to minimize the incoherent noise anyhow present in the recordings (Foti et al., 2015). “Stacked” seismic sections, with greater signal-to-noise ratio, were hence obtained.

After this stacking operation, vertical and transversal component seismograms were combined to derive seismic sections equivalent to a pure vertical or shear excitation. In fact, the hammer blows exerted on the slant faces of the wedge apply a two-component excitation to the ground: a vertical

and a horizontal component, the direction of the latter depending on which face of the plate the stroke is given. Therefore, by summing the seismic traces obtained hitting the wedge on the two sides, the effects of the horizontal components are mutually eliminated, while the vertical components interact constructively; by computing the difference of the corresponding seismograms, the vertical components nullify each other, while the horizontal components interact constructively (Schmelzbach et al., 2016; Sollberger et al., 2016). Consequently, the sum operator is equivalent to the use of a vertical blow; the difference operator is equivalent to a pure shear source.

As examples, we show in Figure 6 the seismic sections derived by summing the vertical component traces (left) and by subtracting the transversal component traces (right) originating from hammer blows on the two opposite sides of the wedge plate, positioned at src1; the first seismogram is equivalent to the section that would be obtained with a vertical blow, the second is equivalent to the section that would be obtained with a shear excitation.

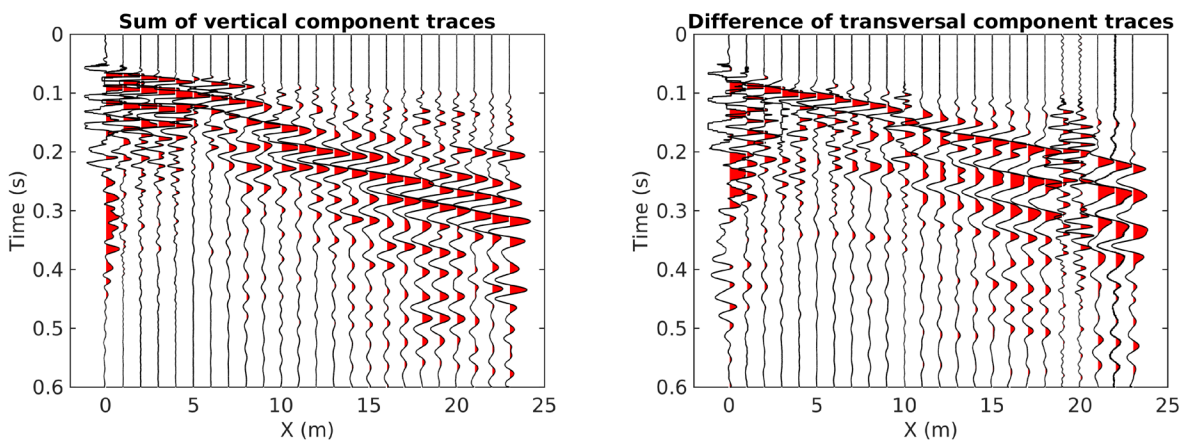


Figure 6 – Seismograms obtained by summing the vertical component traces (left) and by subtracting the transversal component traces (right) originating from hammer blows on the two opposite sides of the wedge plate, positioned at src1. The X coordinate refers to the distance from the westernmost receiver.

3.4.2 Refraction processing and interpretation

P-wave first-break arrival times were manually picked on the seismograms derived by summing the vertical component traces originating from hammer blows on the two opposite sides of the wedge plate, positioned at the same source location. The complete set of obtained travel-time curves (one from each considered shooting position) is shown in Figure 7, top left panel. The hodocrones appear to be approximately symmetrical, i.e. the P-wave travel time depends only on the source-to-receiver distance and not on the position of the shot point. This suggests a 1D geometry (no or little lateral variations) for the near-surface below the active seismic arrays.

As for SH-wave arrivals, these were picked on the seismic sections obtained by computing the difference between the transversal component seismograms recorded when hitting the wedge-shaped plate on the two opposite faces (see previous subsection). The complete set of four SH-wave hodocrones (one from each considered shooting position) is displayed in Figure 7, top right panel. Here again, the picked travel times do not suggest the presence of significant lateral variations.

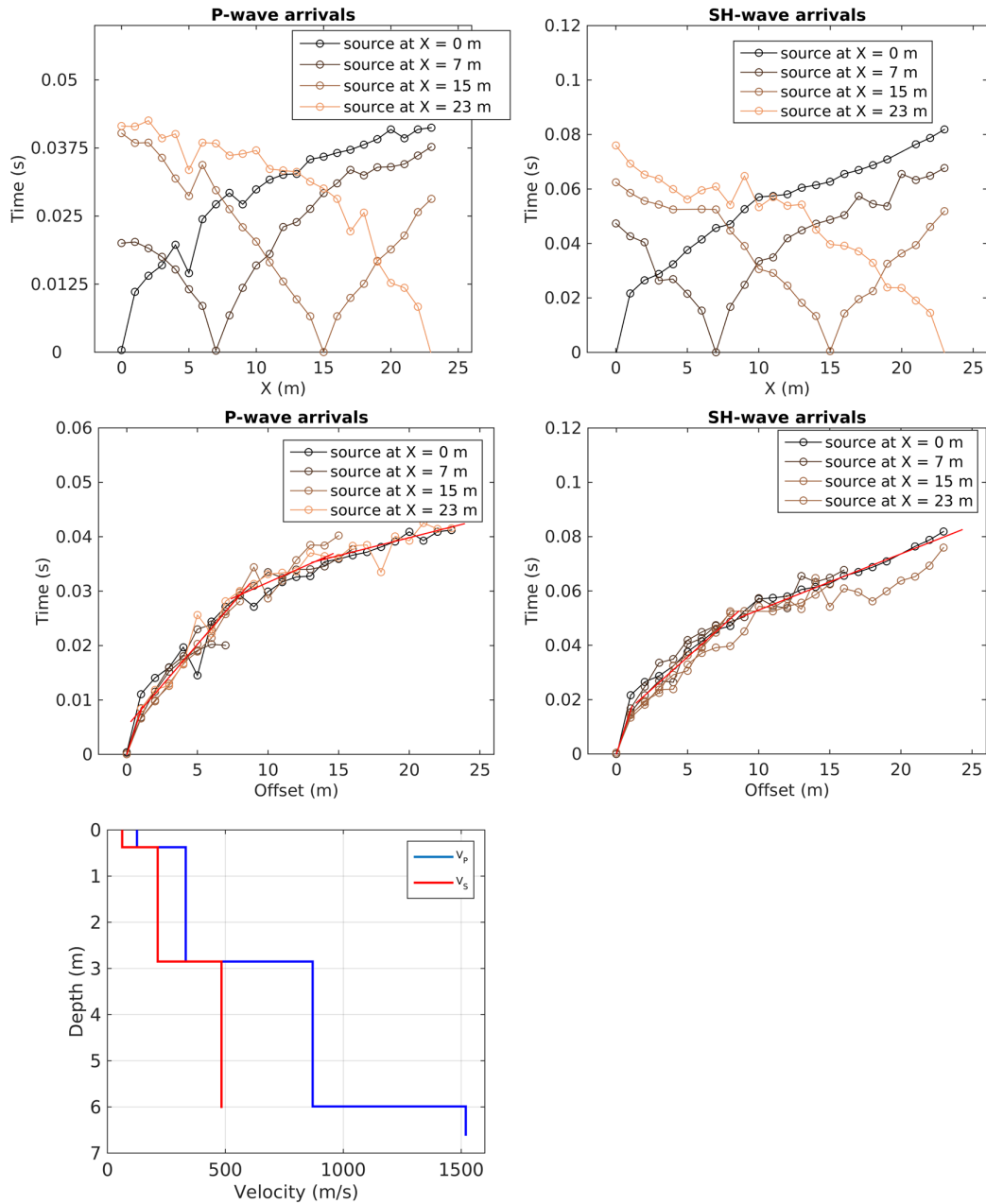


Figure 7 – P- and SH-refraction processing. Top: picked P- and SH-wave first break arrival times. Center: travel-times are collapsed into a single time-offset hodocrone and interpreted with intercept-time method (red lines). Bottom: obtained shallow V_S and V_P profiles.

Collected refraction data were interpreted with the method of intercept time analysis (Reynolds, 2011). Following the hypothesis of a 1D geometry for the shallow subsurface (see above), the hodocrones obtained from refraction processing (Figures 7, top panels) were collapsed into two travel-time curves (one for P-waves, one for SH-waves) in time-offset domain (Figure 7, central panels). The resulting surficial velocity profiles are shown in Figure 7, bottom panel. As for P-waves, a 3-layer+halfspace model was obtained, with V_P increasing from 125 (surface) to around 1500 m/s (6 m depth); as for S-waves, a 2-layer+halfspace model was obtained, whose interfaces agree with the V_P profile.

3.4.3 Rayleigh wave data f - k processing

Rayleigh wave dispersion data were extracted from the vertical and radial component seismograms for MASW acquisitions, recorded when using the sledgehammer vertically striking the flat plate, positioned at src5 (Figure 3). The considered seismic sections were processed by means of a 2D f - k (frequency – wavenumber) transform (Socco and Strobbia, 2004), in order to obtain a conversion of the recorded sets of traces from time–offset to frequency–wavenumber domain. f - k panels from single shot records with the same source position were summed to obtain spectral images with greater S/N ratio (O’Neill, 2003; Neduczka, 2007). The energy maxima corresponding to the Rayleigh wave dispersion curves were picked on these stacked panels; spectral amplitude peaks from individual shot recordings were identified as well, and used to define the uncertainty intervals in the estimation of phase velocities (Socco et al., 2009; Boiero and Socco, 2010).

Figure 8 shows the stacked f - k panels from the considered seismic records, as well as the corresponding picked energy maxima. As expected for a stiff site, the dispersion image is quite fragmented. It is possible to identify two dispersive events, although split into various segments (see also the phase velocity vs frequency representation in Figure 9): the slowest event, extending from 12 to 60 Hz, presents phase velocities gradually decreasing from 600 to 150 m/s, and it was identified as fundamental mode. A second, faster branch spans the frequency band 25 – 60 Hz, with a sharp increase of velocity at ~ 27 Hz, from 400 to 1000 m/s; it was attributed to the first higher mode of Rayleigh wave propagation.

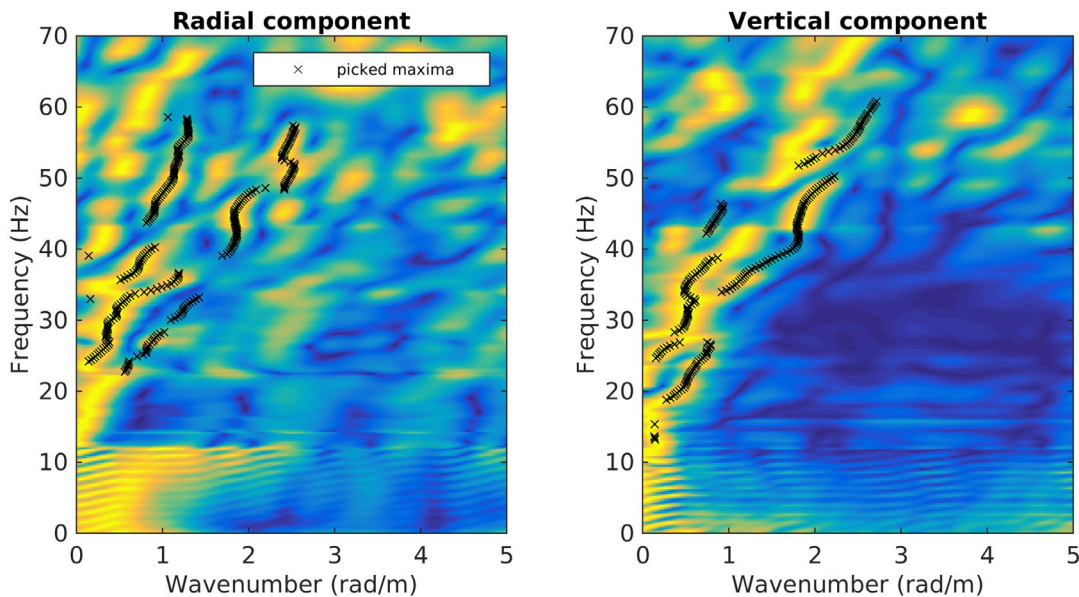


Figure 8 – Stacked f - k spectra obtained from vertical and longitudinal components of the seismic section with source positioned in src 5. The spectral amplitudes are normalized frequency by frequency, so that yellow indicates the maximum amplitude and dark blue corresponds to the minimum amplitude. Black crosses are the picked maxima, corresponding to Rayleigh wave dispersion curve data points.

The two Rayleigh wave dispersion curves from the vertical and radial component of recording were merged into a single curve, representative for the investigated site; as anticipated, the curves derived from each individual shot were exploited to estimate the phase velocity uncertainty intervals (Figure 9).

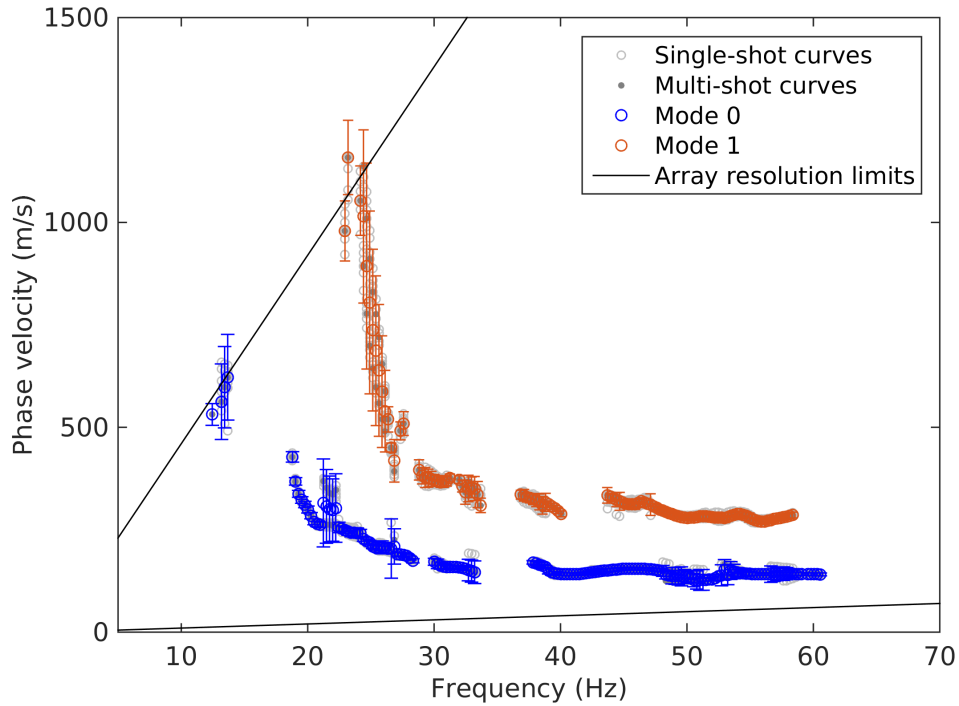


Figure 9 – Rayleigh wave dispersion curve obtained from f - k processing. The curve was obtained merging the two multi-shot curves picked from the stacked vertical and longitudinal component f - k spectra (Figure 8). Dispersion curves from individual-shot f - k panels were used for the estimation of the uncertainty intervals.

3.4.4 WaveDecActive

Seismic traces acquired when using the sledgehammer vertically hitting the flat plate at src5 were also processed with the WaveDecActive code (Maranò et al., 2017), with the aim of retrieving the properties of Rayleigh wave propagation in terms of both phase velocity and ellipticity. WaveDecActive implements a maximum likelihood algorithm for the analysis of Rayleigh waves generated by a controlled source. Differently from the more conventional f - k analysis approach (3.4.3), it is able to characterize the Rayleigh wave propagation in terms of both phase velocity and ellipticity angle. Key parameters required by WaveDecActive are the definition of the maximum number of Rayleigh waves that the code attempts to identify, and the value of parameter γ , which is able to modify the approach of the code towards wave identification from a Bayesian information criterion ($\gamma=1$) to a maximum likelihood approach (ML, $\gamma=0$), or a compromise between the two ($0<\gamma<1$). Following the recommendations of the code’s author (Maranò, 2016) and some preliminary attempts, the maximum number of waves was set to 5, and γ to 0.15, thus opting for an approach close to a maximum likelihood solution.

The obtained results are displayed in Figure 10, top panel, showing the estimated Rayleigh wave phase velocities and ellipticity angles from the considered shots.

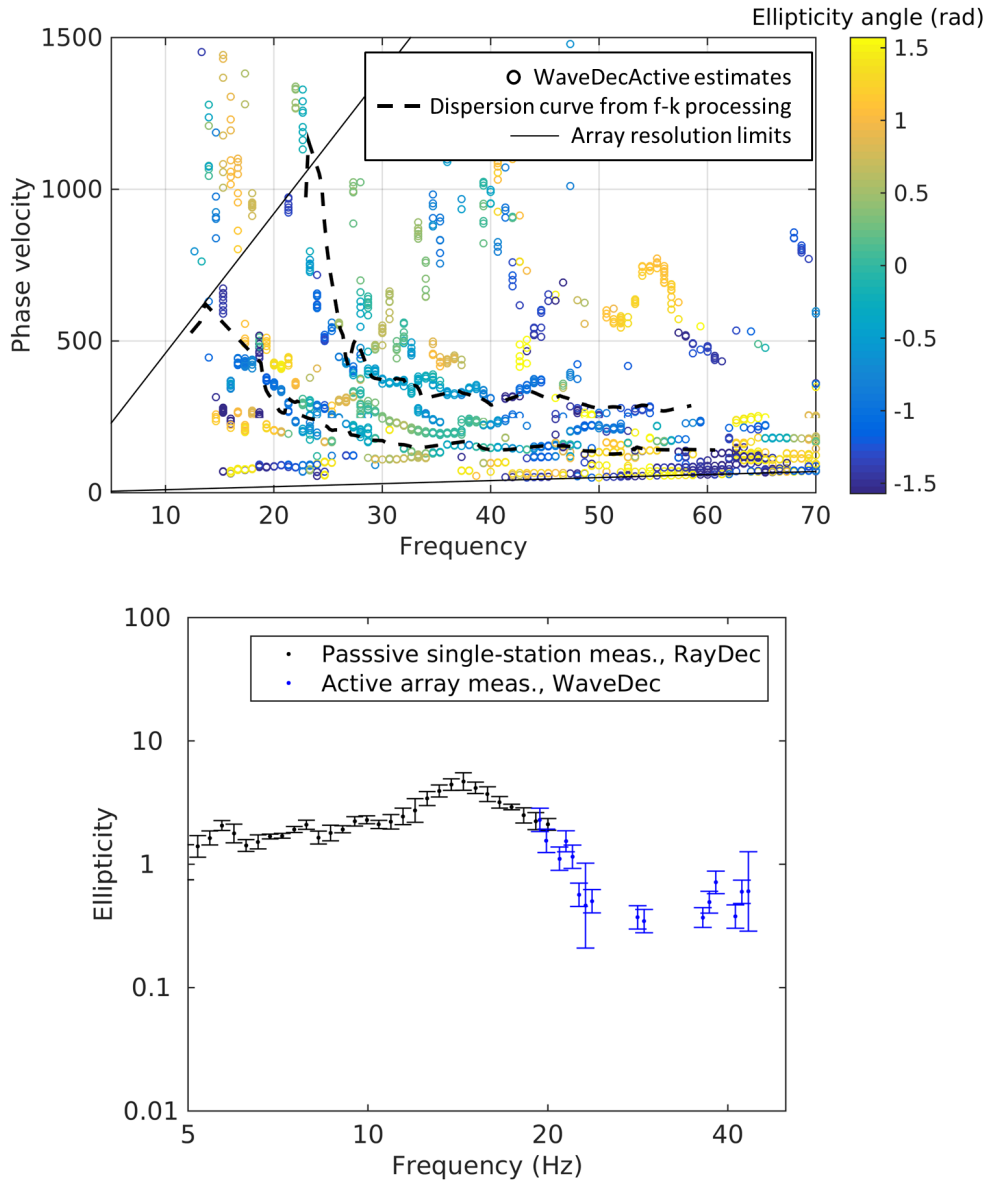


Figure 10 – Extraction of Rayleigh wave dispersion and ellipticity curve with WaveDecActive. Top: joint estimates of phase velocity and ellipticity angle provided by WaveDecActive (colored circles); the dispersion curve obtained from the f-k processing of the same seismic data is shown as a black dashed line. Bottom: Fundamental mode ellipticity curve obtained with WaveDecActive (blue dots). In black dots, the ellipticity curve obtained processing with RayDec (Hobiger et al., 2009) the single-station passive recordings.

Despite the fact that we filtered out, at each frequency, all the estimates with amplitude below the 10th percentile of the overall population, the results seem anyway quite confused, with many, segmented dispersive events. The relatively bad results are probably due to the stiffness of the investigated site, unsuitable for the development of clear Rayleigh wave propagation patterns; as already experienced in similar cases (e.g. Michel et al., 2017 and Bergamo et al., 2017) WaveDecActive does not perform well in these conditions, while f-k analysis is somehow able to provide some results. However, when superimposing the dispersion curve from f-k analysis (dashed black line in Figure 10, top panel), it is possible to identify two branches following approximately the fundamental and first higher mode. We picked the (negative) ellipticity angle estimates along the

Rayleigh wave fundamental mode to obtain the corresponding ellipticity curve (Figure 10, bottom). Interestingly, the obtained curve joins quite well at around 18 Hz with the ellipticity curve derived processing with RayDec (Hobiger et al., 2009) the single-station passive recordings (see next section).

4 Passive seismic measurements

4.1 Acquisition

Besides active seismic surveys, a single-station noise recording measurement was performed. A Lennartz 3C 5s seismometer, connected to a Quanterra Q330 datalogger, was deployed in close proximity to station SCAS2 (Figure 3). The sensor was placed on a metal tripod in a 10 cm deep hole, for a better coupling with the ground. The sampling frequency was 200 Hz, and the recording spanned a 1-hour time interval (after the active survey).

4.2 Processing

The acquired passive traces were processed with the aim of

- estimating the H/V ratio of recorded noise, thus identifying the fundamental frequency of resonance of the site (Nakamura, 1989), thanks to the application of classical H/V methods (as implemented in Geopsy software, www.geopsy.org; classical H/V of Fäh et al., 2001).
- estimating the ellipticity of Rayleigh wave as a function of frequency, by resorting to refined algorithms (Raydec, Hobiger et al., 2009; time-frequency method, Poggi and Fäh, 2010; wavelet-based time-frequency method as implemented in Geopsy software). These methods aim at eliminating the contributions of other waves besides Rayleigh waves, to obtain a more reliable estimation of Rayleigh wave ellipticity when compared to the classical H/V technique.

The obtained results are shown in Figure 11. All applied techniques yield similar H/V or ellipticity curves, with a pronounced peak (identified as fundamental frequency) at 14.65 Hz. At lower frequencies some sharp spikes and troughs can be identified (at 1.1, 1.4, 4.7 and 6 Hz); their appearance suggests an anthropogenic origin. The analysis of the power spectral density of the individual components confirms this hypothesis (Figure 12); at these frequency abscissae we observe extremely consistent features which are likely to be ascribed to man-made sources (e.g. water pumps).

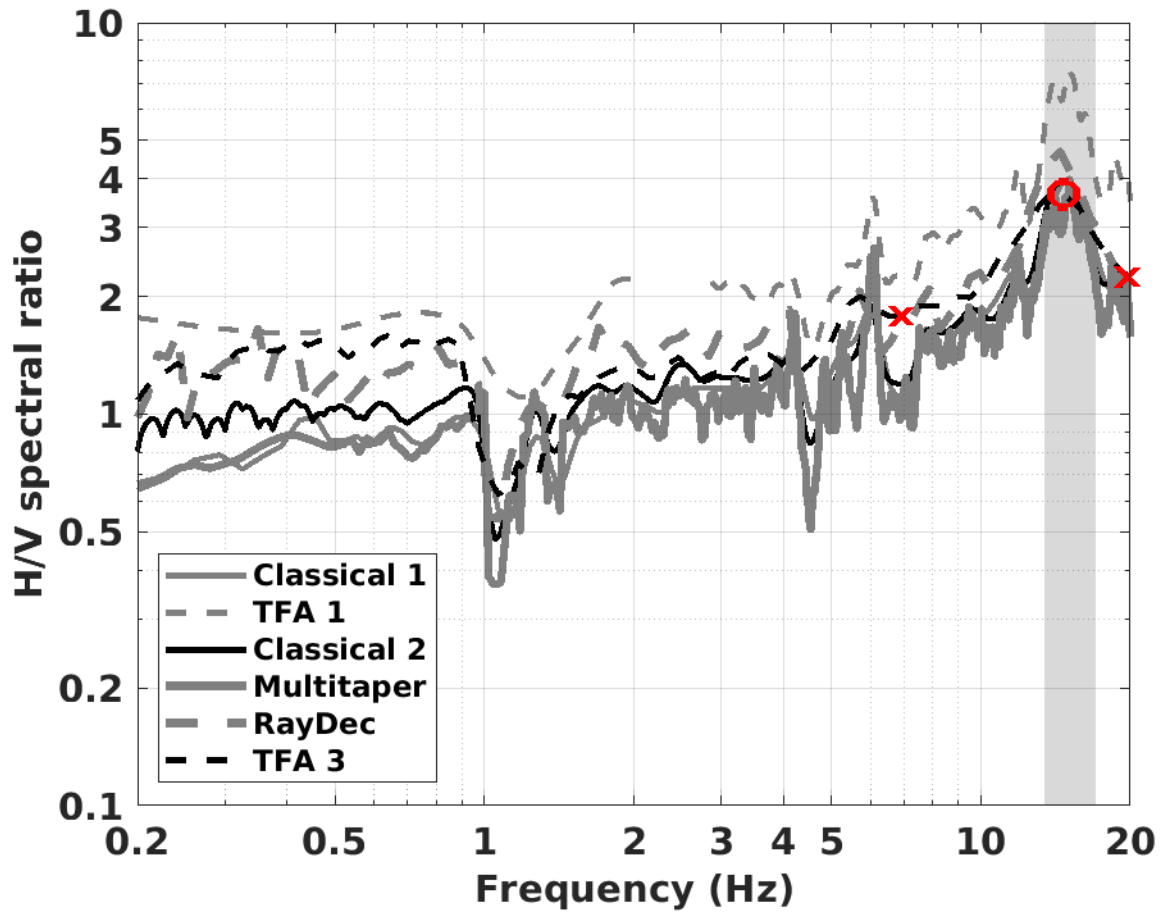


Figure 11 - H/V ratio and ellipticity curves obtained from the processing of noise recording data, using several algorithms. Classical 1: Geopsy; Classical 2: Fäh et al., 2001; TFA1: wavelet-based time-frequency method as implemented in Geopsy software; TFA3: time-frequency method, Poggi and Fäh, 2010; Raydec: Hobiger et al., 2009. The picked resonance frequency is indicated by the red circle.

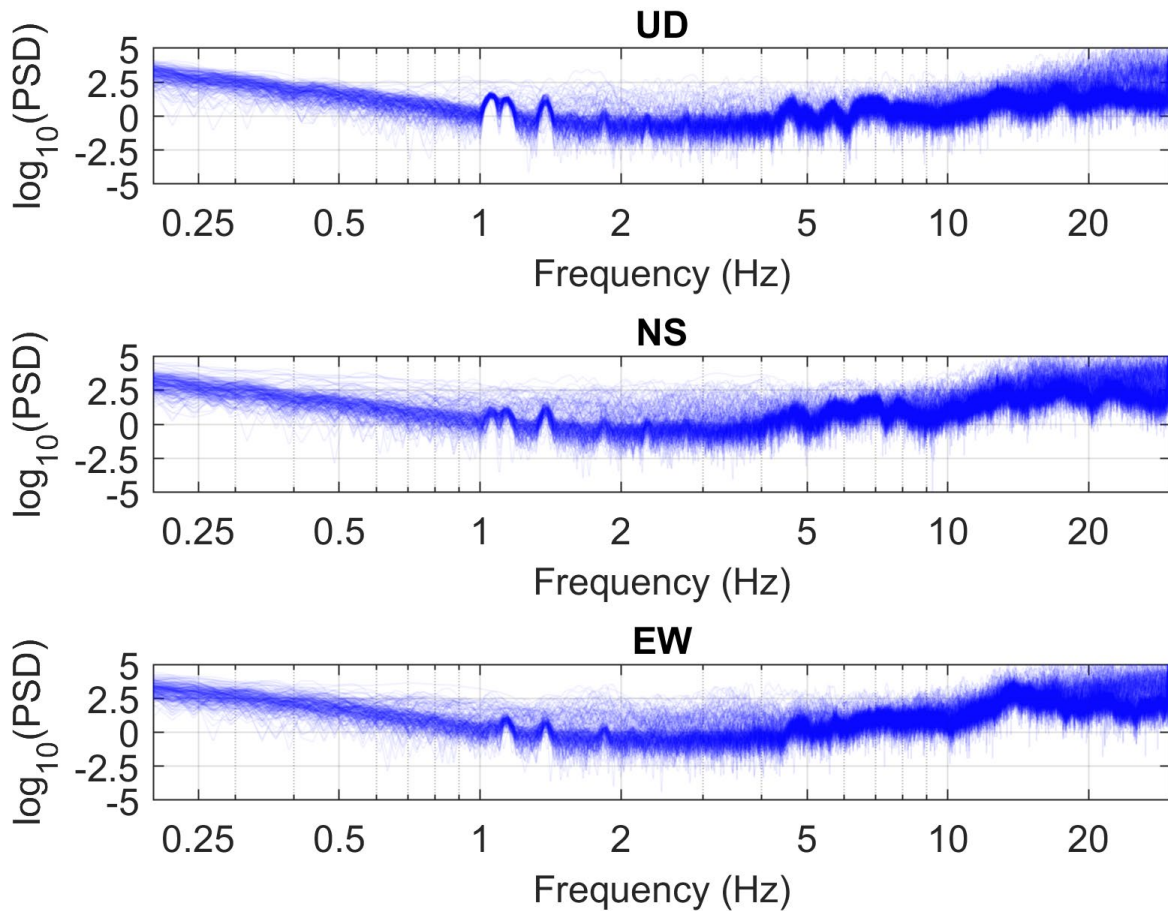


Figure 12 – Power spectral density (PSD) analysis of the three components of the passive recordings (UD=up-down, NS=north-south, EW=east-west). The PSD of each time window of 30 s is represented with a semi-transparent blue line. Note the sharp peaks or troughs at 1.1, 1.4, 4.7 and 6 Hz.

The recordings from the passive sensor were also processed with the polarization tool of Burjanek et al. (2010). Figure 13 shows the ellipticity (as defined in Burjanek et al., 2010) vs. frequency graph. The anthropogenic peaks at 1.1 and 1.4 Hz of Figure 11 present anomalous spikes reaching an ellipticity value of approx. 0.5; vice-versa, the anthropogenic peaks at 4.7 and 6 Hz show ellipticity troughs at circa 0.25, and are characterized by a marked directionality in the NE-SW axis (see polar-strike graph in Figure 14). The fundamental peak of 14.65 Hz (Figure 11) is characterized by a moderate E-W directionality (Figure 14); the site is not considered as hosting significant 2D resonance effects.

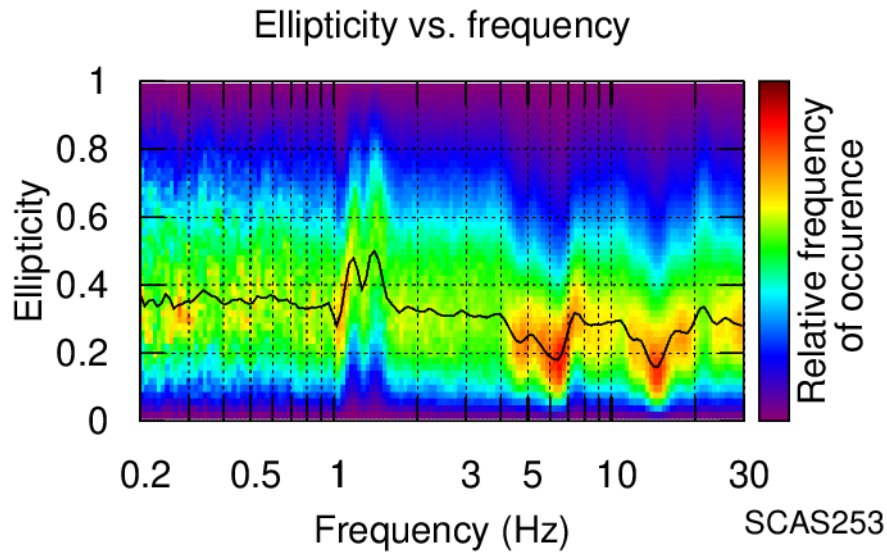


Figure 13 – Ellipticity vs. frequency graph of the passive recording.

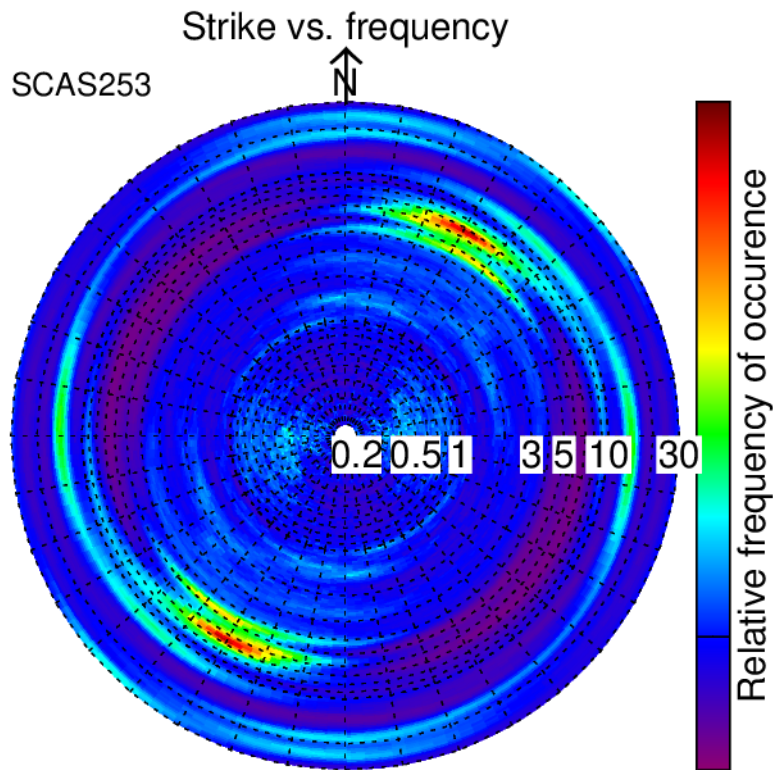


Figure 14 – Polar strike vs. frequency graph of the passive recording.

5 Inversion of Rayleigh wave data

The Rayleigh wave dispersion and ellipticity curves obtained from the processing of active and passive seismic data (see subsections 3.4 and 4.2) were inverted for the 1D S-wave velocity profile of the investigated site. For the inversion we used an ad-hoc code we implemented in Matlab ®. The code performs a Monte Carlo inversion, first generating a population of possible joint V_s/V_p profiles, then computing the synthetic curves corresponding to each model, and finally evaluating the misfit

with respect to the experimental curves. For the solution of the forward problem we resorted to the suite “Computer Programs in Seismology” by Hermann (2013).

5.1 Inversion target

In detail, the target we selected for the inversion consists of:

- The multimodal Rayleigh wave dispersion curve, as obtained from the processing of active data with f-k technique (section 3.4.3); see Figure 15, left.
- The Rayleigh wave ellipticity curve for the fundamental mode from the processing of active data with WaveDecActive code (Figure 10). At low frequency (< 18 Hz), this curve was joined with the ellipticity curve obtained from the single-station passive recording processed with Raydec (see section 4.2). This curve was hence attributed to the fundamental mode of Rayleigh wave propagation. For the inversion we used its data points from 18 down to 6.25 Hz, so to include the ~ 14.5 Hz peak; the portion below 6.25 Hz was discarded as it is not accompanied by any information about Rayleigh wave phase velocity (the dispersion curve extends down to 12.5 Hz only); furthermore, as explained in 4.2, below 6 Hz we have anomalous features in the ellipticity and H/V curves from passive recordings.

The peak at 14.5 Hz in the ellipticity curve was truncated so to allow the modelling of a singularity (Hobiger et al., 2013); see Figure 15, right panel.

The phase velocity and ellipticity curves were resampled on a logarithmically-spaced frequency vector with 100 elements between 5 and 60 Hz.

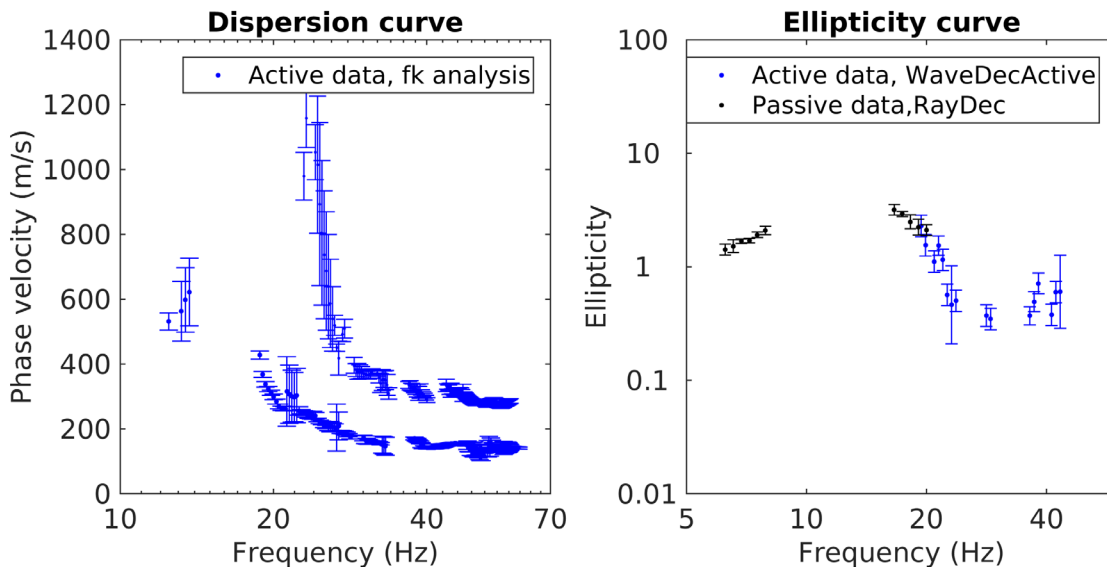


Figure 15 – Target of the surface wave data inversion process. Left: multimodal Rayleigh wave dispersion curve. Right: fundamental mode Rayleigh wave ellipticity

Considering the different frequency bands covered by phase velocity (12.5 – 60 Hz) and ellipticity data (5 – 43 Hz), partly overlapping, the intent is to exploit mainly the dispersion curve information for a detailed characterization of the very shallow subsurface, and to rely on the lower frequency ellipticity points to better constrain the interface between unconsolidated sediments and the underlying gneiss.

5.2 Parameterization of the subsurface

For the parameterization of the subsurface model, after a number of preliminary tests, two different strategies were followed, modeling the soil column as a stack of either 6 or 5 homogeneous layers with variable thickness over a halfspace. In both parameterizations, at each layer, the V_s can vary within broad Monte Carlo boundaries; the same applies to V_p , although the resulting V_s/V_p ratio must be compatible with a range of possible values of Poisson's ratios set for each layer: 0.2-0.4 for the two shallowest formations, 0.2 – 0.49 for the following intermediate layers (to allow for the presence of water-saturated materials, as maybe indicated by refraction results, Figure 7), 0.2 – 0.35 for the two lowest formations. Bulk density values are attributed a priori to each layer, and they increase from 1.9 t/m³ for the weathering formation to 2.2 t/m³ for the halfspace. For the three deepest layers (four or five, depending on the parameterization), S-wave velocity values are forced to be larger than that of the formation above.

For both strategies, we ran an inversion process testing 10⁶ randomly generated models in total. The results are shown and commented in the following section.

5.3 Inversion results

In Figures 16-19, we show the results obtained from each of the two inversion runs (Figure 16,17: 5 layers + halfspace parameterization, Figure 18,19: 6 layers + halfspace parameterization). The two parameterizations achieve similar levels of compliance to experimental data (the minimum RMS error is 1.32 for 6-layer parameterization, 1.33 for 5-layer parameterization; compare Figures 16 and 18). The two sets of profiles are similar as well, although some differences can be identified: the velocity models with 5 layers + halfspace place the interface between weathered and fresher rock at ~12 m, slightly below their 6 layers + halfspace counterparts; also, the latter profiles gradually reach higher values of V_s at depth.

As final result for the inversion, we merged the 10 lowest-misfit velocity models from each parameterization (Figure 20).

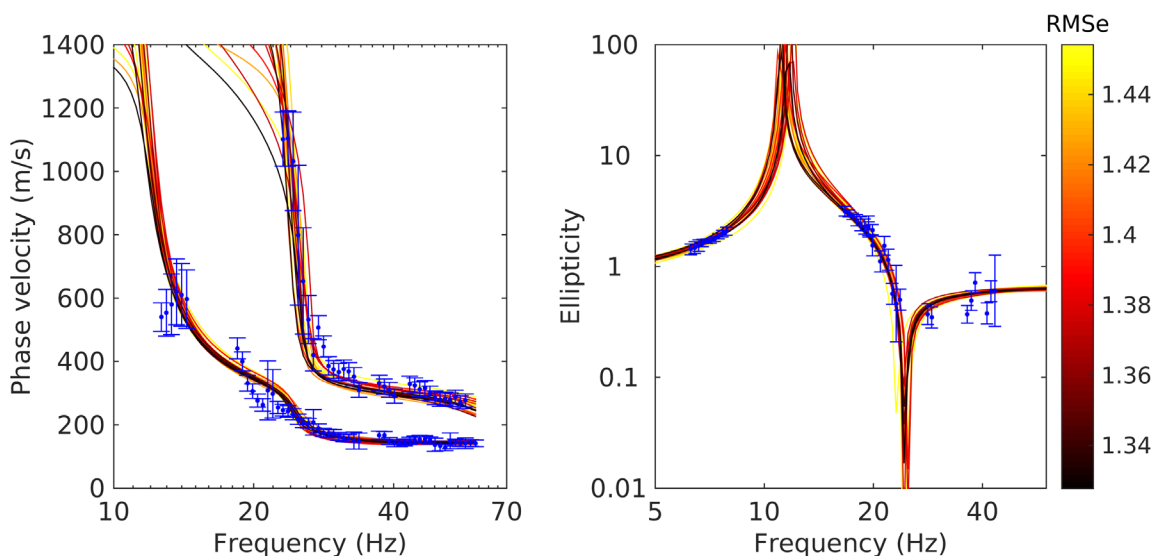


Figure 16 – Fit of experimental Rayleigh wave dispersion and ellipticity curves (blue dots) achieved by the 20 lowest-misfit velocity models (5-layer parameterization).

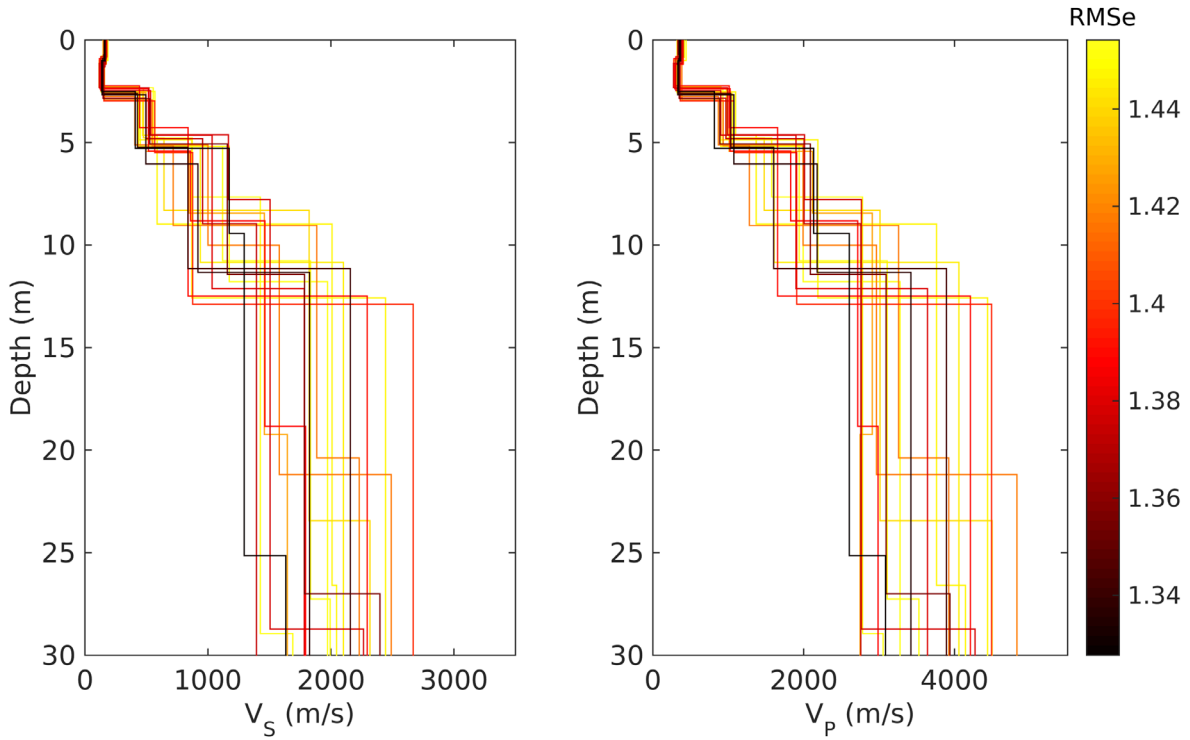


Figure 17 – 20 lowest-misfit velocity models, 5-layer parameterization.

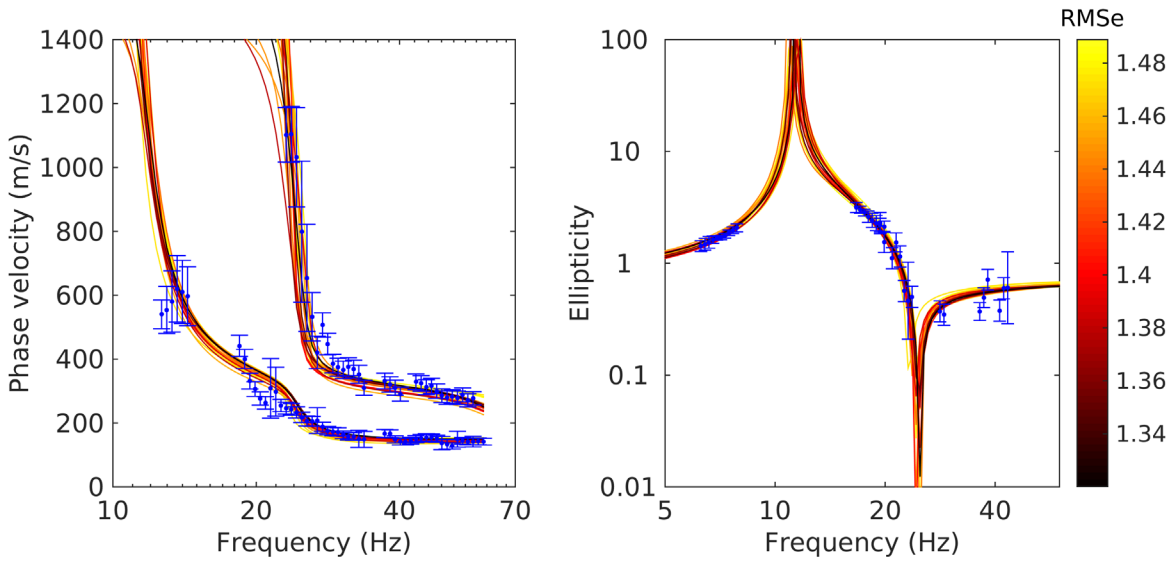


Figure 18 – Fit of experimental Rayleigh wave dispersion and ellipticity curves (blue dots) achieved by the 20 lowest-misfit velocity models (6-layer parameterization).

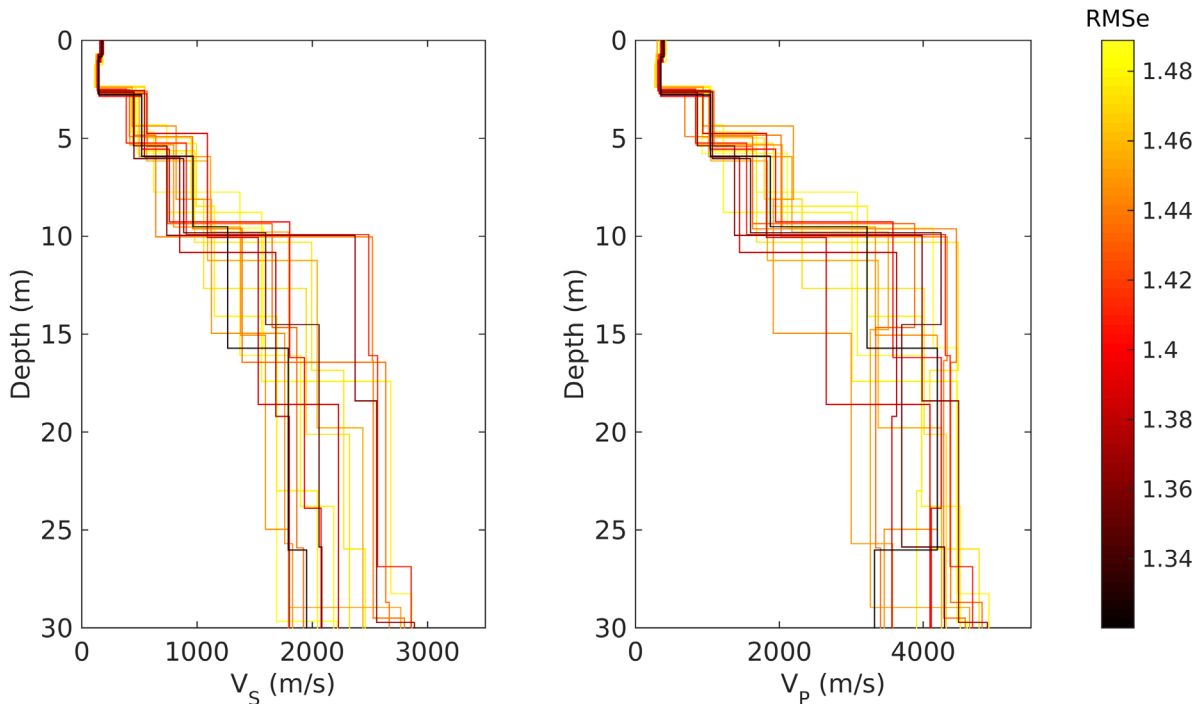


Figure 19 – 20 lowest-misfit velocity models, 6-layer parameterization.

6 Interpretation of the velocity profiles

6.1 Velocity profiles

As anticipated, the final result of the inversion process is a set of 20 velocity models, obtained merging the 10 lowest-misfit profiles from both parameterizations (Figure 20).

At the surface, the uppermost layer is about 2.6 m thick and has a V_s around 150 m/s; below, S-wave velocity increases to ~ 500 m/s, down to a depth of 5 m. These two shallow formations correspond to unconsolidated sediments; further below, a layer of weathered rock is met ($V_s \approx 875$ m/s), with a thickness of about 6 m. We remark that for both S- and P-waves there is a good agreement between velocities estimated from refraction data and from the inversion of Rayleigh wave curves (Figure 20, red lines). Furthermore, the depth of bedrock estimated from Rayleigh wave data, 5 m, is in good agreement with the value (3.8 m) proposed by the sediment-to-bedrock interface reconstruction by Klingelé (2012) at SCAS2 location.

At depths larger than 12 – 13 m the scatter of velocity values among the selected profiles becomes wider, most likely because these depths are no more robustly constrained by Rayleigh wave dispersion curve data. Estimated S-wave velocities are confined within the interval 1500 – 2500 m/s, with values around 2000 m/s representing the center of the distribution. This layer between 11-12 m and the maximum depth of investigation (~ 30 m) is to be associated with relatively intact gneiss.

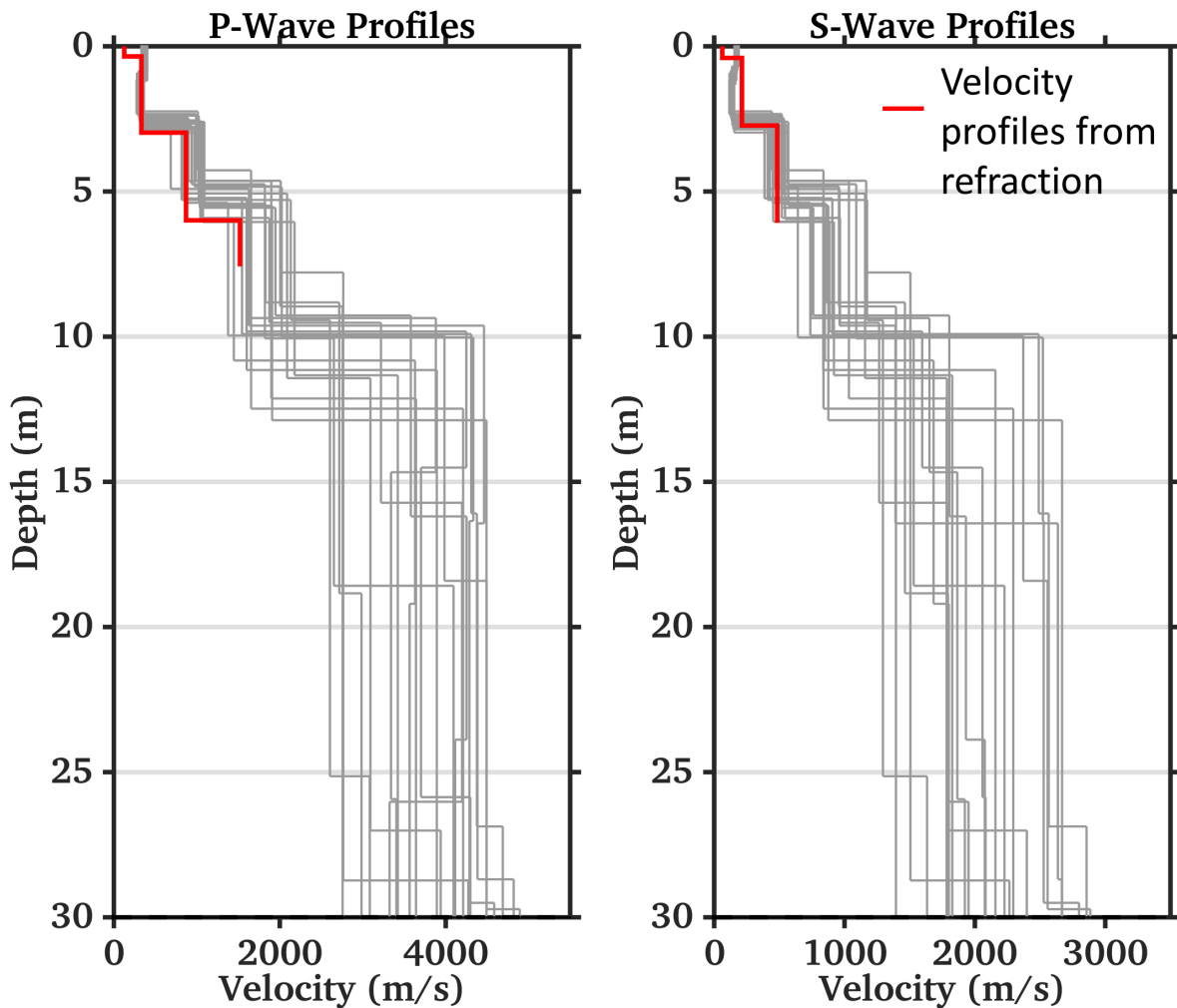


Figure 20 – Final inversion results: 10 best velocity models from each of the two parameterization (gray lines). In red, the velocity models obtained from the interpretation of refraction data (see section 3.4.2).

6.2 Quarter-wavelength representation

The quarter-wavelength velocity representation (V_s^{QWL} ; Joyner et al., 1981) attributes to each frequency the average velocity at a depth equal to $\frac{1}{4}$ of the corresponding wavelength. V_s^{QWL} can be used as direct proxy for the local site characterization, as it physically relates the resolution on ground parameters with the characteristics of the propagating wave-field at the discrete frequencies. The derived quarter-wavelength impedance contrast (IC^{QWL} ; Poggi et al., 2012) is the ratio between two quarter-wavelength average velocities, from the top and bottom part of the velocity profile respectively, at a given frequency; it is a powerful tool to assess the influence of resonance phenomena in soft sediment sites.

Figure 21 shows the average (over the population of the selected 20 best subsurface models) quarter-wavelength velocity (centre) and impedance contrast (bottom) representations. The obtained V_{s30} (which is the average velocity corresponding to a quarter-wavelength of 30 m) is 768 m/s (with an uncertainty interval of 28.5 m/s).

The IC^{QWL} graph shows one peaks at ~ 13 Hz, to be associated with the impedance contrast at 11 - 12 m depth between weathered and compact rock.

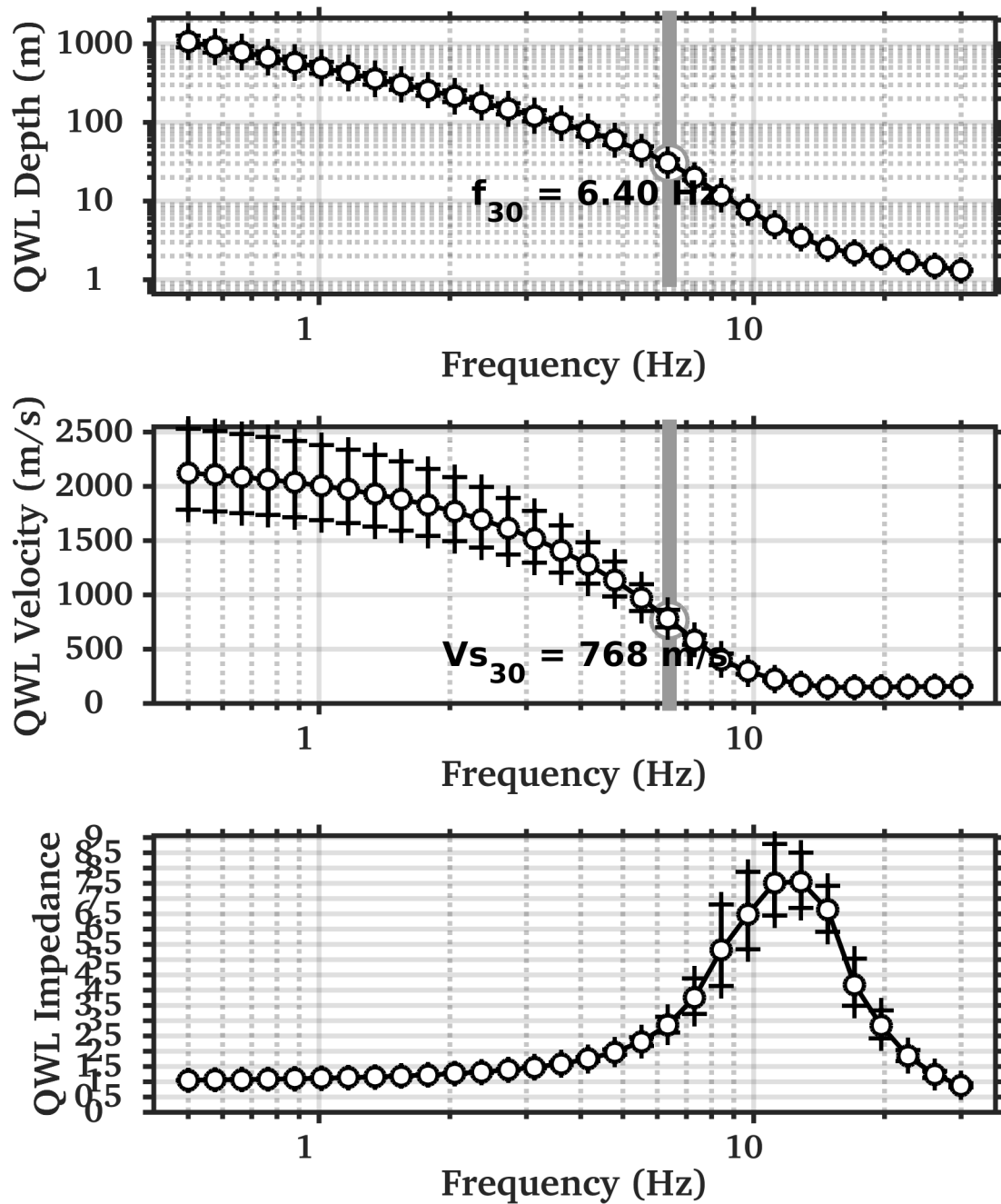


Figure 21 – Average quarter-wavelength representation of the selected velocity profiles (Figure 20). Top: depth; center: velocity; bottom: impedance contrast. The gray line in the top and center panel refers to V_{s30} .

6.3 SH amplification function.

The theoretical SH-wave transfer functions for vertical propagation (Roesset, 1970) were computed for each of the selected models (Figure 20), and then averaged. The resulting mean transfer function was then corrected for the Swiss reference rock model (Poggi et al., 2011).

This synthetic function is compared (Figure 22) with the empirical amplification function obtained from spectral modeling (ESM; Edwards et al., 2013), relying on ~50 events in the 2 – 7 Hz frequency band, decreasing to about 10 events at lower and higher frequencies (as of 16.10.2019).

The synthetic and empirical amplification curves agree in defining a frequency band of higher amplification between 7 – 17 Hz; however, in the empirical function in this frequency range two peaks (8.5 and 13 Hz) can be identified, while the simulated function models a single peak (at 11.5 Hz). The empirical amplification function shows also a minor peak at around 1 Hz, which probably corresponds to an impedance contrast well below the maximum investigation depth of our surveys (about 30 m).

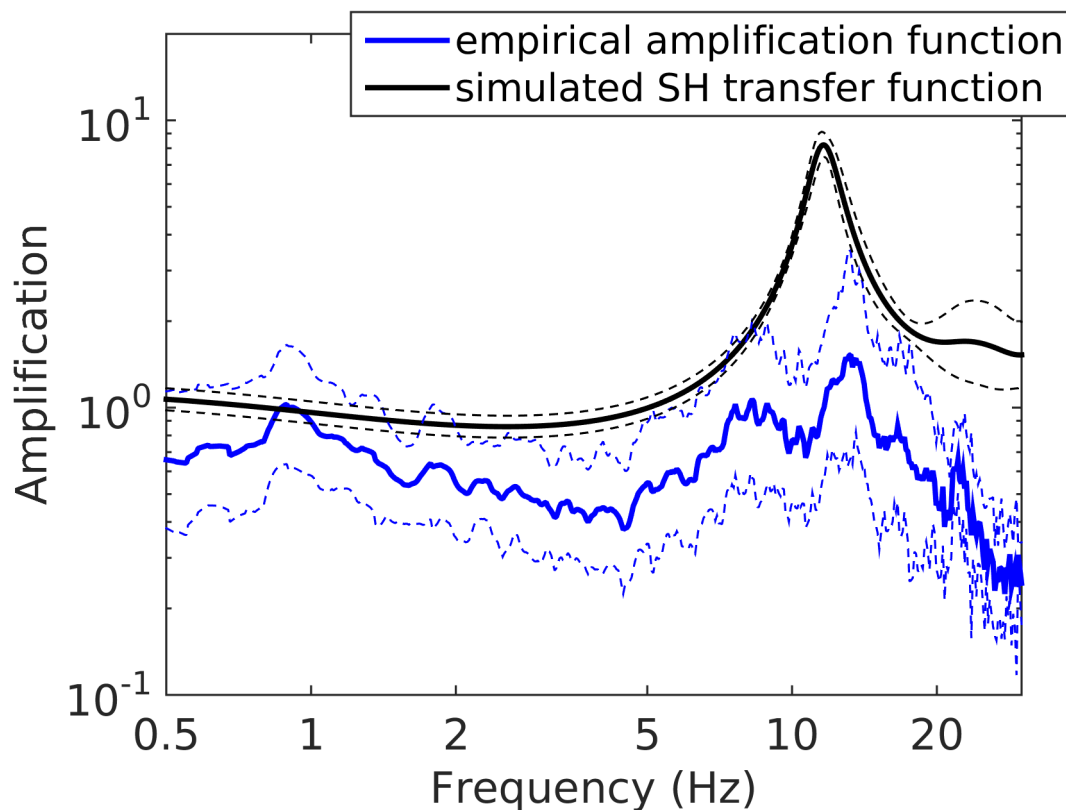


Figure 22 – Average of the modeled SH transfer functions from the selected velocity profiles, corrected (black line) for the Swiss reference rock model, compared with the empirical amplification function for SCAS2 (blue line).

7 Conclusions

Active seismic measurements and a single-station noise recording were performed to characterize the structure of the subsurface below the SSMNet station SCAS2 (Camedo, Centovalli, TI). Active data were processed to derive Rayleigh wave dispersion and ellipticity curves, and to identify the first-

break arrivals of P- and SH-waves (later interpreted with intercept-time method). Passive data were analyzed to estimate the ellipticity curve of Rayleigh waves. Rayleigh wave dispersion and ellipticity curves were inverted for the S-wave velocity profile at the station location.

The obtained velocity profile is as follows: at the surface, the uppermost layer is about 2.6 m thick and has a V_s around 150 m/s; below, S-wave velocity increases to ~ 500 m/s, down to a depth of 5 m. These two shallow formations correspond to unconsolidated sediments; further below, a layer of weathered rock is met ($V_s \approx 875$ m/s), with a thickness of about 6 m. The deepest reconstructed formation (between 11-12 m and the maximum depth of investigation, ~ 30 m) shows S-wave velocities around 2000 m/s, and it is to be associated with relatively intact gneiss.

The sharp velocity contrast at around 11-12 m depth, at the interface between weathered and intact rock, is likely to correspond to the fundamental frequency peak (14.65 Hz) identified in the H/V_{noise} curve.

The estimated V_{S30} value is 768 m/s, which places the site at the upper bound of B class both for SIA261 (SIA, 2014) and Eurocode 8 (CEN, 2004) norms. The engineering bedrock (H800) is estimated at 5 m depth.

Acknowledgements

The authors thank Dario Chiappa and Mauro Häusler for the help in the data acquisition.

References

Bergamo P., M. Hobiger and D. Fäh, 2017. Site characterization report, STSW2 – Lac de Tseuzier (VS). Swiss seismological service (SED)

Boiero, D., and L. V. Socco, 2010, Retrieving lateral variations from surface wave dispersion curves analysis: *Geophysical Prospecting*, **58**, 977–996

Burjanek J., G. Gassner-Stamm, V. Poggi, J.R. Moore and D. Fäh, 2010. Ambient vibration analysis of an unstable mountain slope, *GJI*, 180, 820-828.

CEN, 2004. Eurocode 8: Design of structures for earthquake resistance – Part 1: general rules, seismic actions and rules for buildings. European Committee for Standardization, en 1998-1 edition.

Edwards, B., Michel, C., Poggi, V., and Fäh, D., 2013. Determination of Site Amplification from Regional Seismicity: Application to the Swiss National Seismic Networks. *Seismological Research Letters*, 84(4).

Fäh, D., F. Kind, and D. Giardini, 2001. A theoretical investigation of average H/V ratios. *GJI*, 145, no. 2, 535-549.

Foti, S., Lai C.G., Rix G.J., and C. Strobbia, 2015, *Surface Wave Methods for Near-Surface Site Characterization*: CRC Press, Taylor & Francis Group LLC

Herrmann, R. B. (2013) Computer programs in seismology: An evolving tool for instruction and research, *Seism. Res. Lettr.* **84**, 1081-1088, doi:10.1785/0220110096

Hobiger, M., C. Cornou, M. Wathelet, G. Di Giulio, B. Knapmeyer-Endrun, F. Renalier, P.Y. Bard, A. Savvaidis, S. Hailemichael, N. Le Bihan, M. Ohrnberger, and N. Theodoulidis, 2013. Ground structure imaging by inversion of Rayleigh wave ellipticity: sensitivity analysis and application to European strong motion sites. *GJI*, 192, 207-229.

Hobiger, M., P.-Y. Bard, C. Cornou, and N. Le Bihan, 2009. Single station determination of Rayleigh wave ellipticity by using the random decrement technique (Raydec). *GRL*, 36, L14303

Ivanov, J., R. D. Miller, J.B. Dunbar, and J. Stefanov, 2004. Interrogating levees using seismic methods in southern Texas. *SEG Int'l Exposition and 74th Annual Meeting*, Denver, 10-15 October 2004. *Expanded Abstracts*, 23, 1413-1416.

Joyner, W. B., Warrick, R. E., and Fumal, T. E. (1981). The effect of Quaternary alluvium on strong ground motion in the Coyote Lake, California, earthquake of 1979. *Bulletin of the Seismological Society of America*, 71(4):1333–1349.

Klingelé E., 2012. Systematic analysis of gravity anomalies in Switzerland. *Swiss Geophysical Commission (Ed.). – Annual Report*.

Marano' S., 2016. http://mercalli.ethz.ch/~marra/WaveDec/userguide_WaveDec.html

Marano', S., Hobiger M., P. Bergamo and D. Faeh, 2017. Analysis of Rayleigh Waves with Circular Wavefront: a Maximum Likelihood Approach. *GJI*, 210, 1570-1580.

Michel C., P. Bergamo, A. Lontsi, M. Hobiger, and D. Fäh, 2017. Site characterization report SFRU: Fribourg (FR) – Université. *Swiss Seismological Service (SED)*.

Nakamura, Y., 1989. A Method for Dynamic Characteristics Estimation of Subsurface Using Microtremor on the Ground Surface. *Quarterly Report of RTRI*, vol. 30, no. 1, 25- 33.

Neducza, B., 2007, Stacking of surface waves: *Geophysics*, 72, 51–58.

O'Neill, A., 2003, Full-waveform reflectivity for modelling, inversion and appraisal of seismic surface wave dispersion in shallow site investigations: PhD thesis, University of Western Australia, Perth, Australia.

Park, C. B., R. D. Miller, and J. Xia, 1999. Multichannel analysis of surface waves: *Geophysics*, **64**, 800–808.

Poggi, V., B. Edwards and D. Fäh, 2011. Derivation of a Reference Shear-Wave Velocity model from Empirical Site Amplification. *BSSA*, 101, no. 1, pp. 258-274

- Poggi, V., B. Edwards and D. Fäh, 2012. The quarter-wavelength average velocity: a review of some past and recent application developments. 15th WCEE, Lisbon 2012.
- Poggi, V., and D. Fäh, 2010. Estimating Rayleigh wave particle motion from three component array analysis of ambient vibrations. *GJI*, 180, no. 1, 251-267.
- Redpath, B. B., 1973, Seismic refraction exploration for engineering site investigations: National Technical Information Service, Technical Report E-73-4.
- Reynolds, J.M., 2011, An introduction to applied and Environmental Geophysics: John Wiley & Sons, Ltd.
- Roesset, J. (1970). Fundamentals of soil amplification. In Hansen, R. J., editor, *Seismic Design for Nuclear Power Plants*, pages 183–244. M.I.T. Press, Cambridge, Mass
- Schmelzbach C., D. Sollberger, S. A. Greenhalgh, H. Horstmeyer, H. Maurer and J.O.A. Robertsson, 2016. 9C seismic data acquisition for near-surface applications: recording, wavefrom reciprocity and 4C rotation. 78th EAGE conference and exhibition. Extended abstract WS04 B0
- SIA, 2014. SIA 261 Einwirkungen auf Tragwerke. Société Suisse des ingénieurs at des architectes, Zurich, Switzerland.
- Socco, L.V., and C. Strobbia, 2004, Surface-wave method for near-surface characterization: a tutorial: *Near Surface Geophysics*, **2**, no. 4, 165-185.
- Sollberger D., C. Schmelzbach, C. Van Renterghem, J. O. Robertsson and S. A- Greenhalgh, 2016. Single-component elastic wavefield separation at the free surface using source- and receiver-side gradients. SEG International Exposition and 86th annual meeting, 2268 – 227
- Swisstopo, Service géologique national, 2018. Atlas géologiques de la Suisse 1 :25000 : 1312 feuille de Locarno
- Swisstopo, 2019. Thickness model of unconsolidated deposits (available at <https://map.geo.admin.ch>)